LETTER

doi:10.1038/nature11987

A syringe-like injection mechanism in *Photorhabdus luminescens* toxins

Christos Gatsogiannis[1]*, Alexander E. Lang[2]*, Dominic Meusch[1], Vanda Pfaumann[2], Oliver Hofnagel[1], Roland Benz[3], Klaus Aktories[2] & Stefan Raunser[1]

***Photorhabdus luminescens* is an insect pathogenic bacterium that is symbiotic with entomopathogenic nematodes[1]. On invasion of insect larvae, *P. luminescens* is released from the nematodes and kills the insect through the action of a variety of virulence factors including large tripartite ABC-type toxin complexes[2] (Tcs). Tcs are typically composed of TcA, TcB and TcC proteins and are biologically active only when complete[3–5]. Functioning as ADP-ribosyltransferases, TcC proteins were identified as the actual functional components that induce actin-clustering, defects in phagocytosis and cell death[5–7]. However, little is known about the translocation of TcC into the cell by the TcA and TcB components. Here we show that TcA in *P. luminescens* (TcdA1) forms a transmembrane pore and report its structure in the prepore and pore state determined by cryoelectron microscopy. We find that the TcdA1 prepore assembles as a pentamer forming an α-helical, vuvuzela-shaped channel less than 1.5 nanometres in diameter surrounded by a large outer shell. Membrane insertion is triggered not only at low pH as expected, but also at high pH, explaining Tc action directly through the midgut of insects[8]. Comparisons with structures of the TcdA1 pore inserted into a membrane and in complex with TcdB2 and TccC3 reveal large conformational changes during membrane insertion, suggesting a novel syringe-like mechanism of protein translocation. Our results demonstrate how ABC-type toxin complexes bridge a membrane to insert their lethal components into the cytoplasm of the host cell. We believe that the proposed mechanism is characteristic of the whole ABC-type toxin family. This explanation of toxin translocation is a step towards understanding the host–pathogen interaction and the complex life cycle of *P. luminescens* and other pathogens, including human pathogenic bacteria, and serves as a strong foundation for the development of biopesticides.**

To understand ABC-type Tc proteins and, consequently, their mechanism of pore formation and toxin translocation, we used cryo-electron microscopy and single-particle analysis (SPA) to determine the structure of the TcdA1 complex at a resolution of 6.3 Å (Fig. 1 and Supplementary Figs 1 and 2). TcdA1 forms a 17-nm-wide, 25.5-nm-long pentamer with a molecular mass of ~1.41 megadaltons (MDa) (Fig. 1a). The overall bell-like shape of the complex results from an inner, 25.5-nm-long pore that is, for the most part, surrounded by a large outer shell (Fig. 1b). Because the crystal structures of neither full TcA complexes nor subunits are known, we identified all clearly resolved rod-like electron densities and fitted poly-alanine helices into them (Fig. 1c, d). Contrary to previous suggestions[9] that favoured a β-barrel structure as predicted for the pore-forming anthrax protective antigen[10], the channel shows a clear α-helical architecture with 25 central α-helices. In addition, our computational analysis identified five β-sheets in the upper part of the pore (Fig. 1c). Shaped like a vuvuzela (a flared funnel) that narrows from its maximum diameter of 3 nm to less than 1.5 nm, the central pore is composed of an upper, cone-shaped vestibule consisting of at least five β-sheets and five α-helices, and a long, tube-shaped channel formed by two consecutive sets of ten α-helices.

Two large domains per subunit of the pentameric complex form the outer shell. Whereas one contains 26 clearly resolved α-helices, the other is dominated by β-sheets (Fig. 1a, d). To locate these regions in the protein sequence, we performed a sequence-based secondary structure prediction analysis of TcdA1 (Supplementary Fig. 3). We identified a large amino-terminal region spanning amino acids 1–1090, composed mainly of α-helices, followed by a large β-strand-dominated region (amino acids 1091–1720), which corresponds well to our structure. In accordance with our structure for the central pore, the carboxy-terminal region of the protein is composed of exceptionally long α-helices (1721–2320) and short terminal β-strands (2324–2516). Thus, each subunit of the TcdA1 pentamer is composed of an N-terminal α-helical domain, a central β-sheet domain and a C-terminal pore-forming domain (Fig. 1d and Supplementary Video 1).

The exceptional length of the helices in the pore-forming domain (up to 90 amino acids) allowed us to assign their corresponding sequence to them precisely (Fig. 1e). We identified a series of four helices per protomer (2020–2284) arranged as pairs of consecutive long and short helices that run antiparallel to each other to form the wall of the tube.

In our structure, the central pore is closed not only by the loops connecting the pore-forming helices, but also by the outer shell that occludes the lower part of the pore. We therefore conclude that our structure represents the prepore state of TcdA1. To obtain the TcdA1 complex in the pore state, we reconstituted the complex into liposomes (Fig. 2a) and determined its structure at a resolution of 19.9 Å using cryoelectron microscopy and SPA (Fig. 2b–e and Supplementary Fig. 2). We note that the umbrella-like shape of the pore complex differs considerably from that of the bell-like prepore structure. Whereas the latter resembles the structure of Yen-Tc K::9 from *Yersinia entomophaga*[9], the overall shape of the TcdA1 pore complex is similar to the anthrax and α-haemolysin toxin pores[11,12].

To provide a better comparison between pore and prepore, we filtered the prepore structure to 19.9 Å and segmented both maps (Fig. 2f, g). When comparing both structures, very large rearrangements of the major domains between the pore and prepore structure become obvious (Fig. 2f, g and Supplementary Fig. 4a, b). The central pore is shifted by 115 Å towards the lower end of the complex, and its lower tubular part penetrates the membrane. Although the resolution is low, the structure of the pore suggests that it is open at this position. This could be achieved by lateral movement of the transmembrane helices during integration into the membrane (Fig. 2g).

The two domains of the outer shell are rotated and shifted relative to each other in a complex manner that results in a more compact subunit with greater distance to adjacent subunits (Supplementary Fig. 4a, b). Consequently, the outer shell has a larger diameter, is open at both sides and encloses mainly the funnel-like part of the central pore, forming a large basin (Supplementary Fig. 4c–e).

[1]Department of Physical Biochemistry, Max Planck Institute of Molecular Physiology, 44227 Dortmund, Germany. [2]Institut für Experimentelle und Klinische Pharmakologie und Toxikologie, Albert-Ludwigs-Universität Freiburg, 79104 Freiburg, Germany. [3]School of Engineering and Science, Jacobs University Bremen, Campusring 1, 28759 Bremen, Germany.
*These authors contributed equally to this work.

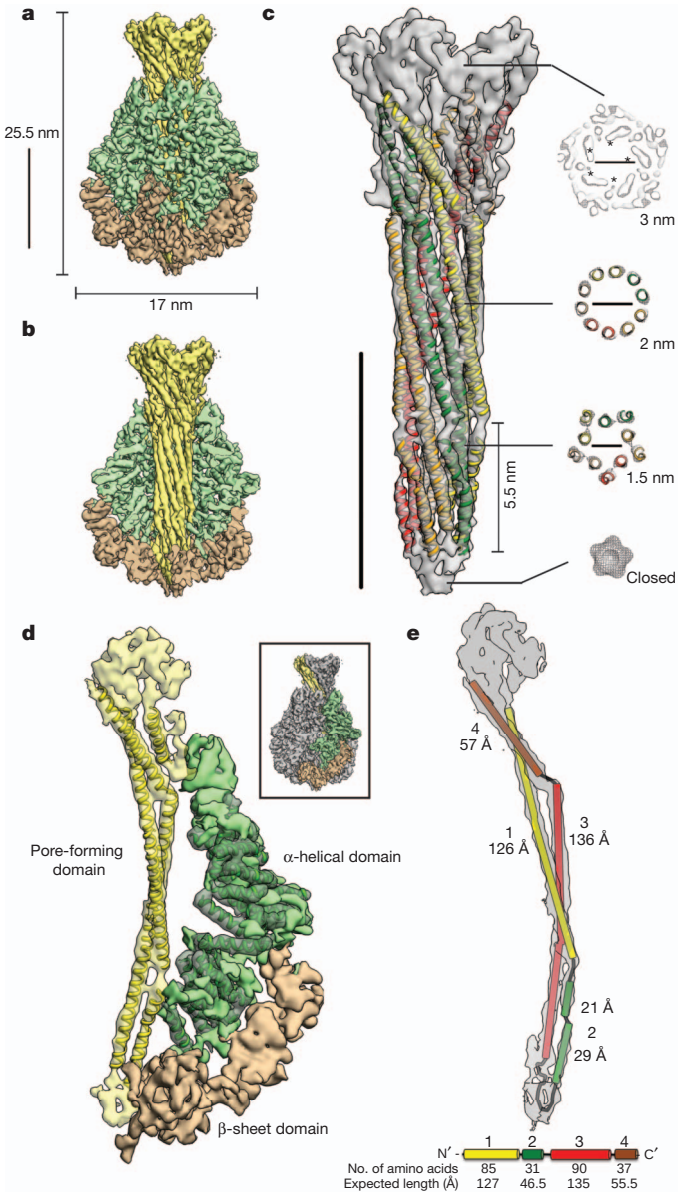

Figure 1 | Cryoelectron microscopy structure of the TcdA1 prepore complex. **a**, Electron density map of the TcdA1 prepore complex. **b**, Cut-away view displaying the central pore. The two domains of the outer shell are respectively depicted in green and brown, and the central pore is depicted in yellow. **c**, Fit of identified α-helices into the electron density of the central pore. At right are shown slices through the central pore at different heights. Asterisks indicate β-sheets. **d**, Extracted electron density of a protomer with identified α-helices. The outlined box shows the localization of the subunit in the complete structure. Densities corresponding to the N-terminal α-helical domain, the central β-sheet domain and the C-terminal pore-forming domain are depicted in green, brown and yellow, respectively. **e**, Sequence assignment to α-helices in the pore-forming domain. The four identified helices are depicted as numbered and coloured cylinders with their respective lengths. At bottom are shown the sequence-based secondary structure prediction for amino acids 2018–2284, the number of amino acids for each predicted helix and the expected lengths of the helices. Helices 1–4 include amino acids 2020–2105, 2109–2140, 2153–2244 and 2249–2285, respectively. Scale bars, 10 nm.

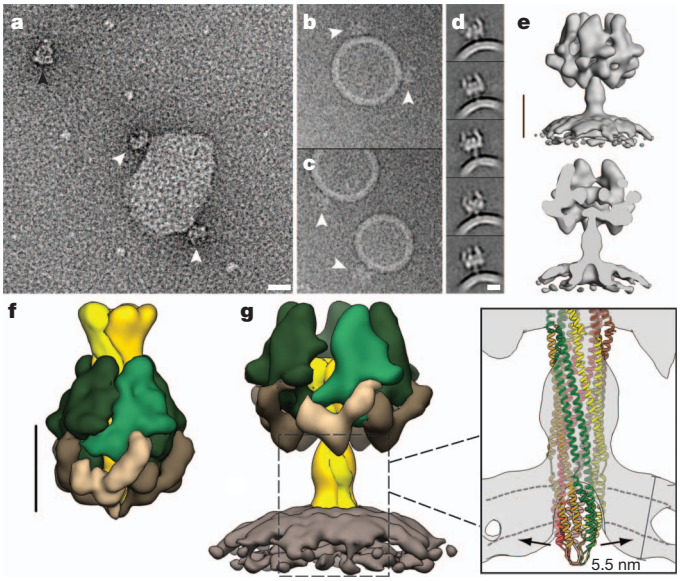

Figure 2 | Cryoelectron microscopy structure of the TcdA1 pore and comparison with the prepore complex. **a**–**c**, Representative fields of negatively stained (**a**) and vitrified (**b**, **c**) TcdA1 complexes reconstituted in liposomes. Black and white arrowheads indicate molecules in the prepore and pore state, respectively. Scale bars, 20 nm. **d**, Representative class averages of the vitrified reconstituted complex. Scale bar, 10 nm. **e**, Cryoelectron microscopy structure of the TcdA1 pore depicted in side and cut-away views. Scale bar, 10 nm. **f**, **g**, Segmentation of maps of the prepore (**f**) and pore (**g**) states; the two domains of the outer shell are respectively depicted in green and brown, and the central channel is depicted in yellow. The cut-away view in the inset in **g** shows that the transmembrane helices need to move laterally to fit into the density and to open the pore. Scale bar, 10 nm.

Our data strongly suggest that TcdA1 is an α-helical pore-forming toxin (α-PFT). Whereas other PFTs form the pore during membrane insertion[13,14], for TcdA1 the pore is already present before membrane insertion, but is shielded by the outer shell of the protein. Surprisingly, although sequence-based hydrophobicity analyses of TcdA1 predict a higher hydrophobicity for the helices inside the membrane (Supplementary Fig. 5a), they do not detect clear transmembrane regions as is the case for other structurally characterized α-PFTs[15]. Structure-based calculations of the surface hydrophobicity potential, however, identify strongly hydrophobic stretches in the predicted transmembrane region (Supplementary Fig. 5b), indicating that the hydrophobicity is increased by the ordered assembly of *per se* moderately hydrophobic α-helices.

In analogy to AB-type toxins, such as anthrax toxin[10], the Tc complex is thought to bind first to a receptor on the cell surface before being undergoing endocytosis[5,9]. On acidification of the endosome, the pH shift induces the insertion of TcA into the endosomal membrane, which translocates either the C component or both the B component and the C component into the cytosol[5,9]. However, *in vitro*, that is, without receptor and membranes, the prepore TcdA1 complex proved to be stable over a wide pH range (pH 4.5 to pH 10) (Supplementary Fig. 6) and insertion into preformed vesicles was difficult, although not impossible. For more extreme pH values, such as pH 4, we observed many aggregates, but many of the non-aggregated complexes resembled the pore state of the complex (Supplementary Fig. 6a). Surprisingly, a shift to high pH values, such as pH 11, also induced pore formation of TcdA1 *in vitro* (Supplementary Fig. 6e). Depending on protein concentration, we also observed monomers, dimers and tetramers of pentamers (Supplementary Fig. 6e). This effect is probably caused by the interaction of the exposed hydrophobic transmembrane regions and was also observed in other pore-forming toxins[16].

Comparing the structure of this complex obtained by negative-stain electron microscopy and SPA with the negative-stain electron microscopy structure of the prepore complex (Fig. 3a, b) and with the reconstituted complex in liposomes (Fig. 2e) proves that the complex indeed represents the pore state of TcdA1. The observed extreme pH values needed for the transition probably result from the absence of the receptor. Nevertheless, our experiments show that a pH shift induces the transition from the prepore state of TcdA1 to the pore state

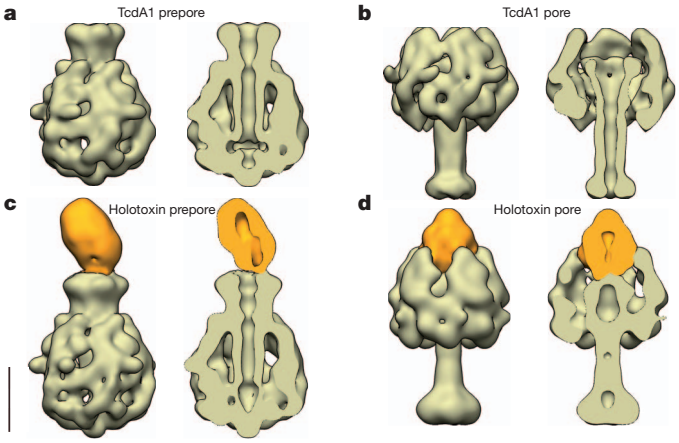

Figure 3 | Structure of the PTC3 holotoxin complex. Side views and central cuts of negatively stained TcdA1 and the PTC3 holotoxin complex in the prepore and pore states. **a**, Prepore TcdA1; **b**, pore TcdA1; **c**, prepore PTC3 holotoxin complex; **d**, pore PTC3 holotoxin complex. TcdA1 and TcdB2–TccC3 are shown in khaki and orange, respectively. Scale bar, 10 nm.

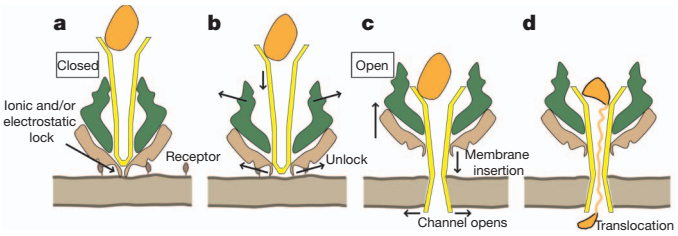

Figure 4 | Syringe-like mechanism for membrane insertion. Model for membrane insertion of the PTC3 complex and translocation of the B–C complex. The two domains of the outer shell are respectively depicted in green and brown, and the central pore of TcdA1 is depicted in yellow. The dimeric complex of TcdB2 and TccC3 is depicted in orange. The beige bar indicates the membrane bilayer. **a**, The PTC3 complex is either taken up orally or secreted into the haemocoel, where it binds to a yet unknown receptor and is endocytosed. **b**, **c**, Lowering the pH in the endosome or increasing the pH in the insect gut destroys an ionic and/or electrostatic lock in the outer shell of the TcdA1 pentamer. The outer shell is then structurally reorganized. As a result, it widens and releases the central pore (**b**), which penetrates the membrane like a syringe (**c**). The pore opens and at the same time the B–C complex is pulled into the basin formed by the funnel of the central pore and the outer shell of the TcdA1 complex. **d**, There, it is unfolded and transported through the central pore.

(Supplementary Fig. 7a–d and Supplementary Video 2). As described for many G-protein-coupled receptors, lowering the pH, with resulting protonation of residues, very probably destroys ionic as well as electrostatic interactions and thereby causes conformational changes[17]. Our finding that a shift to higher pH values results in the same transition indicates that deprotonation of residues, and not only their protonation, can release the ionic or electrostatic lock that constrains the TcdA1 complex in its prepore conformation.

In accordance with our observations for TcdA1 reconstitution in liposomes, lipid bilayer experiments demonstrated that TcdA1 formed ion-permeable channels over a large pH range (pH 4 to pH 11), exhibiting a well-defined single-channel conductance (Supplementary Fig. 8a–c). As expected from our electron microscopy studies, the pore-forming activity of TcdA1 was higher at extreme pH values. At pH 11, the pore-forming activity of TcdA1 was more than 100-fold greater than at pH 6. This probably explains why Tc toxins also directly intoxicate the midgut[8], which is highly alkaline in many insects[18]. However, in nature the nematodes release *P. luminescens* only in the haemocoel[19], where it first colonizes midgut cells, which presumably endocytose the lethal bacterial toxins[20]. Although it is tempting to speculate that the ability to form a pore at both low and high pH values would allow Tc toxins to intoxicate midgut cells in two ways, from the haemocoel and at the same time from inside the gut, the process in nematodes suggests that this mechanism might not be used in nature.

We measured the TcdA1 pore when reconstituted into a bilayer and, in line with our cryoelectron microscopy structure, found that the TcdA1 pore is funnel shaped with an entrance diameter of 3.0 nm and a minimum diameter of about 1.6 nm (Supplementary Figs 8d and 9 and Supplementary Table 1). This result corroborates our structural data, showing that the central pore of TcdA1 is already formed in the prepore state and does not change much during membrane insertion.

To determine where the B and C subunits bind to the A subunit, we first assembled the B and C subunits and then assembled the full PTC3 holotoxin, composed of TcdA1, TcdB2 and TccC3, and determined their structures by electron microscopy and SPA (Fig. 3c, d, Supplementary Fig. 7e–h and 10). The TcdB2 and TccC3 subunits form a strong, dimeric, oval-shaped complex (Supplementary Fig. 10). Corresponding well with biochemical data of the Tc complex from *Xenorhabdus nematophilus*[4], only one B–C complex rather than five binds to a TcdA1 pentamer directly interacting with the funnel-shaped vestibule of the TcdA1 channel (Fig. 3c). pH-induced pore formation of TcdA1 as described above results in the insertion of the B–C complex into the basin formed by the outer shell and the funnel of the inner channel (Fig. 3d). However, we did not observe its partial or full translocation through the TcdA1 pore, which probably requires a proton or other electrochemical gradient across the membrane, and/or chaperones.

The information provided by these structures allows us to propose the following mechanism for membrane insertion of TcdA1 and protein translocation. First the fully assembled holotoxin composed of TcdA1, TcdB2 and TccC3 is either taken up orally or secreted into the haemocoel of the insect, where it binds as a prepore to a yet unknown receptor at the cell surface and is endocytosed (Fig. 4a). At that time, the pore is closed and shielded by the outer shell of the protein. A pH-sensitive ionic and/or electrostatic lock opens on acidification of the endosome or on alkalization of the insect gut (Fig. 4b). As a result, the outer shell widens and releases the central pore, which penetrates the membrane like a syringe (Fig. 4c). The pore opens and at the same time the B–C complex is pulled into the basin formed by the central pore and the outer shell, inducing its unfolding and translocation (Fig. 4d and Supplementary Video 3). The structural data on TcdA1 and PTC3 described here reveal that ABC-type toxins are exceptional α-PFTs that insert into membranes using a unique syringe-like mechanism. Hence, it serves as a strong foundation for understanding the action of other pathogens, including human pathogenic bacteria.

METHODS SUMMARY

TcdA1 and TcdB2–TccC3 were recombinantly expressed in *Escherichia coli* BL21-CodonPlus and purified using Ni-IDA affinity as well as size-exclusion chromatography. Membrane insertion and pore activity was measured using black lipid membranes composed of diphytanoyl phosphatidylcholine. For electron microscopy, the samples were applied to carbon-coated or holey-carbon grids either stained with 0.07% uranyl formate or vitrified. Negatively stained complexes were imaged with a JEOL JEM-1400 electron microscope equipped with a LaB_6 cathode operated at 120 kV. Digital electron micrographs were recorded with a 4k × 4k CMOS camera F416 (TVIPS) using minimal-dose conditions. Images of vitrified complexes were made with a JEOL JEM 3200FSC electron microscope equipped with a field-emission gun at an operating voltage of 200 kV. An in-column omega energy filter was used to improve image contrast by zero-loss filtering with a slit width of 15 eV. Micrographs were recorded with an 8k × 8k TemCam-F816 CMOS camera (TVIPS) under minimal-dose conditions (15–20 electrons per $Å^2$). The SPARX software[21] was used for all image-processing steps with the exception of the initial defocus determination, which was done using CTFFIND3[22] (Supplementary Figs 2, 11–14). To identify α-helices, we used the programs PHENIX[23] and VOLTRAC[24]. For visualization and analysis, we used CHIMERA and implemented programs[25]. Sequence-based secondary structure analysis was carried out using the SABLE protein structure prediction server (http://sable.cchmc.org/). A detailed description of our methods can be found in Supplementary Information.

Received 22 September 2012; accepted 5 February 2013.
Published online 20 March 2013.

1. Joyce, S. A., Watson, R. J. & Clarke, D. J. The regulation of pathogenicity and mutualism in Photorhabdus. *Curr. Opin. Microbiol.* **9,** 127–132 (2006).
2. ffrench-Constant, R. H. & Bowen, D. J. Novel insecticidal toxins from nematode-symbiotic bacteria. *Cell. Mol. Life Sci.* **57,** 828–833 (2000).
3. Waterfield, N. R., Bowen, D. J., Fetherston, J. D., Perry, R. D., &. ffrench-Constant, R. H. The tc genes of *Photorhabdus*: a growing family. *Trends Microbiol.* **9,** 185–191 (2001).
4. Sheets, J. J. *et al.* Insecticidal toxin complex proteins from *Xenorhabdus nematophilus*: structure and pore formation. *J. Biol. Chem.* **286,** 22742–22749 (2011).
5. Lang, A. E. *et al. Photorhabdus luminescens* toxins ADP-ribosylate actin and RhoA to force actin clustering. *Science* **327,** 1139–1142 (2010).
6. Lang, A. E., Schmidt, G., Sheets, J. J. & Aktories, K. Targeting of the actin cytoskeleton by insecticidal toxins from *Photorhabdus luminescens*. *Naunyn Schmiedebergs Arch. Pharmacol.* **383,** 227–235 (2011).
7. Aktories, K., Lang, A. E., Schwan, C. & Mannherz, H. G. Actin as target for modification by bacterial protein toxins. *FEBS J.* **278,** 4526–4543 (2011).
8. Bowen, D. *et al.* Insecticidal toxins from the bacterium *Photorhabdus luminescens*. *Science* **280,** 2129–2132 (1998).
9. Landsberg, M. J. *et al.* 3D structure of the *Yersinia entomophaga* toxin complex and implications for insecticidal activity. *Proc. Natl Acad. Sci. USA* **108,** 20544–20549 (2011).
10. Young, J. A. T. & Collier, R. J. Anthrax toxin: receptor binding, internalization, pore formation, and translocation. *Annu. Rev. Biochem.* **76,** 243–265 (2007).
11. Katayama, H. *et al.* Three-dimensional structure of the anthrax toxin pore inserted into lipid nanodiscs and lipid vesicles. *Proc. Natl Acad. Sci. USA* **107,** 3453–3457 (2010).
12. Song, L. *et al.* Structure of staphylococcal α-hemolysin, a heptameric transmembrane pore. *Science* **274,** 1859–1865 (1996).
13. Geny, B. & Popoff, M. R. Bacterial protein toxins and lipids: pore formation or toxin entry into cells. *Biol. Cell* **98,** 667–678 (2006).
14. Parker, M. W. & Feil, S. C. Pore-forming protein toxins: from structure to function. *Prog. Biophys. Mol. Biol.* **88,** 91–142 (2005).
15. Iacovache, I., van der Goot, F. G. & Pernot, L. Pore formation: an ancient yet complex form of attack. *Biochim. Biophys. Acta* **1778,** 1611–1623 (2008).
16. Eifler, N. *et al.* Cytotoxin ClyA from *Escherichia coli* assembles to a 13-meric pore independent of its redox-state. *EMBO J.* **25,** 2652–2661 (2006).
17. Ramon, E. *et al.* Critical role of electrostatic interactions of amino acids at the cytoplasmic region of helices 3 and 6 in rhodopsin conformational properties and activation. *J. Biol. Chem.* **282,** 14272–14282 (2007).
18. Dow, J. A. Extremely high pH in biological systems: a model for carbonate transport. *Am. J. Physiol.* **246,** R633–R636 (1984).
19. Milstead, J. E. *Heterorhabditis* bacteriophora as a vector for introducing its associated bacterium into the hemocoel of *Galleria mellonella* larvae. *J. Invertebr. Pathol.* **33,** 324–327 (1979).
20. ffrench-Constant, R, *et al. Photorhabdus*: towards a functional genomic analysis of a symbiont and pathogen. *FEMS Microbiol. Rev.* **26,** 433–456 (2003).
21. Hohn, M. *et al.* SPARX, a new environment for cryo-EM image processing. *J. Struct. Biol.* **157,** 47–55 (2007).
22. Mindell, J. A. & Grigorieff, N. Accurate determination of local defocus and specimen tilt in electron microscopy. *J. Struct. Biol.* **142,** 334–347 (2003).
23. Adams, P. D. *et al.* The Phenix software for automated determination of macromolecular structures. *Methods* **55,** 94–106 (2011).
24. Rusu, M., Starosolski, Z., Wahle, M., Rigort, A. & Wriggers, W. Automated tracing of filaments in 3D electron tomography reconstructions using Sculptor and Situs. *J. Struct. Biol.* **178,** 121–128 (2012).
25. Pettersen, E. F. *et al.* UCSF Chimera–a visualization system for exploratory research and analysis. *J. Comput. Chem.* **25,** 1605–1612 (2004).

Supplementary Information is available in the online version of the paper.

Acknowledgements We are grateful to R. S. Goody for continuous support and for comments on the manuscript. We thank I. Vetter for stimulating discussions. This work was supported by the Deutsche Forschungsgemeinschaft grants RA 1781/1-1 (S.R.) and AK 6/22-1 (K.A.) and by Max Planck Society (S.R.).

Author Contributions A.E.L. and V.P. cloned constructs and purified proteins; D.M. performed pH studies; A.E.L. and R.B. performed and analysed black lipid bilayer assays; C.G. screened samples and collected negative-stain electron microscopy data; C.G. and O.H. collected cryoelectron microscopy data; C.G. processed and refined electron microscopy data; C.G. and S.R. analysed electron microscopy data; K.A. and S.R. designed the study. C.G. and S.R. wrote the paper. All authors discussed the results and commented on the manuscript.

Author Information The coordinates for the electron microscopy structures have been deposited in EMDataBank under accession codes EMD-2297 to EMD-2301. Reprints and permissions information is available at www.nature.com/reprints. The authors declare no competing financial interests. Readers are welcome to comment on the online version of the paper. Correspondence and requests for materials should be addressed to S.R. (stefan.raunser@mpi-dortmund.mpg.de).